EurJIC
European Journal of Inorganic Chemistry

Research Article
doi.org/10.1002/ejic.202200417

Chemistry Europe
European Chemical Societies Publishing

www.eurjic.org

Special Collection

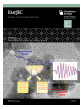

Modeling Heterogeneity in UO_2 Nanoparticles Using X-ray Absorption Spectroscopy

Shinhyo Bang,[a] Dominic R. Russo,[b] Ashley D. Knapp,[a] Mark D. Straub,[b] Kurt F. Smith,[b, c] Corwin H. Booth,[b] Stefan G. Minasian,[b] and Liane M. Moreau*[a]

EXAFS provides the capability to interrogate nanoparticle (NP) structure in atomistic detail without relying on long-range crystallinity. There is a limitation in that EXAFS provides averaged structural information, making it difficult to separate a small amount of heterogeneous structure from bulk. In this work, models were developed to extract surface-specific information from conventional EXAFS measurements collected on UO_2 NPs of varying size. Specifically, the surface terminating species of UO_2 NPs was determined from comparison of coordination numbers with geometric models while the origin of static disorder was interrogated from user-defined simulations. Results show that the degree of oxygenation on the NP surface does not significantly deviate from bulk surface and that static disorder is highly enhanced in NP surface layers but cannot be attributed to surface relaxation effects alone. The approach described herein has the potential to be adapted to a range of inorganic NP systems to interrogate surface structure.

Introduction

The application of nanoscience to actinide (An) chemistry has been crucial in elucidating the transport mechanism of radionuclides in the environment, owing to its pertinence to radioactive contamination.[1] It has been reported that upon the exposure of nuclear materials to environmental conditions, radionuclides (notably U and Pu) can form An oxide nanoparticles (NPs).[1–2] Therefore, a more complete understanding of the synthetic environment of these NPs and their properties will enable more accurate predictions and improved strategies for remediation of radioactive contamination sites. Furthermore, actinide nanochemistry shows promise in the development of advanced nuclear fuel with superior mechanical properties including radiation-damage resistance,[3] which would enhance the safety and efficiency of nuclear power plant operation. UO_2 NPs also require lower sintering temperatures compared with bulk UO_2, which suggests a promising path for reusing actinides from spent nuclear fuel.[4] The potential application of An-containing nanostructures spans beyond the nuclear industry to the development of constructs for targeted alpha-therapy[5] and heterogeneous catalysis.[6]

It is imperative to characterize the structural attributes of these An NPs (both at the NP surface and in the interior) for a better understanding of their behavior due to the intimate connection between structure and resulting properties. The surface structure in particular deserves attention due to its pivotal role in the reactions that take place at the interface, such as adsorption and corrosion.[7] Unfortunately, the surface characterization of An NPs proves challenging due to their radioactivity, which requires encapsulation of the material or dedicated instruments to avoid potential contamination. This fundamentally limits the use of conventional surface-characterization techniques such as X-ray photoelectron spectroscopy (XPS). The ejected photoelectrons from the material surface cannot reach the detector if the material is encapsulated. Even if encapsulation-free photoelectron spectroscopy is possible with a dedicated radiological instrument, this method is not suitable for the characterization of NPs embedded in a matrix or in solution. Also, while the importance of XPS in extracting the surface composition and electronic structure attributes cannot be overstated, XPS requires NPs to be isolated and prepared in the solid state under ultra-high vacuum or below-ambient pressure conditions to extract accurate photoelectron spectra which can be difficult to achieve and may not be representative of the nascent solution environment.[8] High resolution transmission electron microscopy (HRTEM)[9] and scanning tunnelling microscopy (STM)[10] are techniques previously utilized to probe atomic scale arrangements at the NP surface. Both typically rely on the same UHV conditions that limit XPS use and relevant *in-situ* environments. While *in-situ* HRTEM sample holders have been developed,[11] the beam energy is maintained at a high level (often hundreds of keV) to

[a] S. Bang, A. D. Knapp, Prof. L. M. Moreau
Department of Chemistry
Washington State University
Pullman, WA 99164, USA.
E-mail: liane.moreau@wsu.edu
[b] D. R. Russo, M. D. Straub, Dr. K. F. Smith, Dr. C. H. Booth, Dr. S. G. Minasian
Chemical Sciences Division
Lawrence Berkeley Laboratory
Berkeley, CA 94720, USA
[c] Dr. K. F. Smith
Nuclear Waste Services
Building 329 Thompson Avenue, Harwell Campus
Didcot, OX11 0GD, United Kingdom

Supporting information for this article is available on the WWW under https://doi.org/10.1002/ejic.202200417

Part of the "EurJIC Talents" Special Collection.

Research Article
doi.org/10.1002/ejic.202200417

achieve atomic resolution, which often results in beam damage to ultra-small NP samples and significantly limits the ability to measure structure with atomistic confidence.[12] Another challenge in the characterization of NPs is the insensitivity of diffraction-based methods such as X-ray diffraction (XRD) to NP structure due to inherent Scherrer broadening resulting from small grain size and lack of long-range order.[13] Although it will not be discussed in this paper, it should be noted that in contrast to XRD, scattering-based methods such as high-energy X-ray scattering (HEXS) are powerful tools to investigate the structures of amorphous and nanostructured materials which lack long-range order.[14] One shortcoming of scattering techniques, however, is a lack of elemental specificity (unless anomalous methods are used). Element specificity is only a minor issue for the case of actinide oxides, where the actinide species of interest is a much heavier scatterer than oxygen.

Extended X-ray absorption fine structure (EXAFS) spectroscopy has proven an advantageous alternative in the characterization of An NP atomic scale coordination environments because it does not require long-range crystallinity in order to extract local structure.[15] The highly penetrating nature of hard X-rays also aids in overcoming encapsulation barriers and facilitates measurement *in-situ* for NPs confined to solid-state or solution matrices. A key disadvantage to the use of EXAFS for elucidating NP structure, is that it provides the averaged coordination environment of the element of interest within the sample and therefore is not a precise probe of the heterogeneity that may be present. This poses an issue in NP characterization, where the environment of a surface-bound atom differs from that of an atom within the NP interior. Therefore, extraction of accurate structural information from such a heterogeneous system necessitates accurate models of heterogeneity and considerations of their effects on EXAFS spectra. The use of grazing incidence (GI) EXAFS can remove the necessity of these models because it directly provides the surface structure of a material by confining the X-ray field to the first few layers of the surface by varying the incidence angle.[16] However, conventional EXAFS cannot be entirely replaced by GI EXAFS because it requires solid-state samples with low surface roughness. Additionally, the interaction between NPs and a substrate has the potential to affect the structure.[17]

A few key EXAFS-derived models to account for heterogeneity in NPs have already been demonstrated in the NP literature. For example, an accurate description of the undercoordinated nature of NP's surface atoms (also known as the termination effect) successfully predicted the morphology of a NP from the EXAFS-evaluated coordination number (CN).[18] CNs were estimated based on the hypothetical size and shape of NPs, and then compared with the experimental results to backtrack their actual size and shape. These aforementioned methods have predicted the morphology of NPs with a simple geometric consideration (the arrangement of absorbing atoms) that ignores radially dependent heterogeneity, which may occur in layers closer to the NP surface. To account for surface-dependent heterogeneity, Yevick and Frenkel[19] simulated EXAFS spectra based on molecular dynamics-informed surface relaxation models. The similarity between the simulated and experimental EXAFS was used to extract the morphology of NPs[20] and to consider the validity of the atomistic simulation.[21] While this is a powerful method, it has yet to be extended to more complex structures, such as ceramic oxides or bimetallic systems. We believe that insights made through these existing models can be further enhanced by incorporating informed user-defined inputs which will construct radially dependent distance and disorder distributions extending from the NP core to the terminating surface.

Herein, we present a method to extract surface-specific structural information from averaged NP EXAFS spectra by properly modeling the heterogeneity of UO_2 NPs through user-defined heterogeneous inputs informed by size-dependent trends and *a priori* knowledge of bulk UO_2 surface structure. UO_2 NPs were prepared by thermal decomposition of a molecular precursor in covalent organic framework (COF) templates, as has been previously reported.[22] The absence of significant surface ligand interaction and higher surface oxidation for this NP system (as was already investigated in detail in Ref [21] and thus not discussed here) provided an optimal ground to investigate surface structure of spectroscopically clean surfaces. Our primary objective in this work was to develop models to determine surface-terminating species and surface-dependent structural differences for UO_2 NPs in comparison to bulk UO_2 counterparts. This was accomplished through comparison to experimental NP spectra of varying size and developing models that consider a bulk-like *core* and surface-dependent *shell*, such that surface results were preferentially extracted from bulk signal. In particular, user-defined surface relaxation and amorphization effects can be incorporated and fit to experimental data to extract surface-dependent information. Key results of our investigation include: 1) oxygen shielding on the NP surface is present at comparable levels to bulk and 2) surface disorder is appreciably larger than that observed in the NP core, and this trend is more pronounced for smaller NP sizes. Overall, this work provides insight into An NP surface attributes by developing models to extract surface-dependent information from conventional EXAFS. These models can be extended with appropriate system-specific assumptions to describe the structural attributes of inorganic NPs beyond the case of UO_2.

Results

XAFS data show systematic trends as a function of NP size

XAFS spectra were collected at the U L_3 absorption edge for three quasi-spherical UO_2 NP sizes (1.4, 4.7, and 8 nm, refer to the supporting information for more details) as well as bulk UO_2. Since the NP sizes are all below 10 nm, the measurements sampled a large percentage of atoms that reside on the NP surface (60-69% for 1.4 nm, 24–37% for 4.7 nm and 14–22% for 8 nm, with variations accounting for different surface faceting, Table S4). This means that the NPs will be varyingly sensitive to

changes that are imparted due to the presence of surface vs. interior atoms.

From the near edge XANES region of the spectrum, as shown in Figure 1a, all NPs exhibit edge and white line (first main peak) energies indicative of U(IV),[23] which are within ~1 eV of bulk (Table S1). Near edge features also resemble bulk UO_2. One exception is that in all cases, the NP samples exhibit an increased white line peak, which is the main absorption peak after the sharp edge increase. This is not surprising due to the trend for NPs to have a sharpened 5d band, which has previously been attributed to the loss of long-range order at the particle surface.[24] Overall, the NP XANES well-retains the expected characteristics of bulk UO_2, providing support that there is not significant higher oxidation present.

Figure 1b shows $\chi(R)$, the Fourier transform of $k^3\chi(k)$ from the EXAFS region where k is the photoelectron wave vector and $\chi(k)$ the EXAFS function. The dampening of NP $\chi(R)$ peaks with R relative to the bulk displayed in Figure 1b suggests a significant decrease in the CN for NPs with respect to bulk, which are more pronounced for NPs with smaller size.[15d,25] This dampening can be attributed to the surface termination effect. The decrease in amplitude can also indicate increased disorder.[15d,25] The dampening effect of disorder is difficult to decouple from decreased CN due to the high degree of correlation between CN and σ^2. Therefore, great care needs to be taken to collect data with a sufficient k-range and at multiple temperatures. Of great importance to this study was the ability to extract static disorder with confidence by performing Debye analysis as described in the following section.

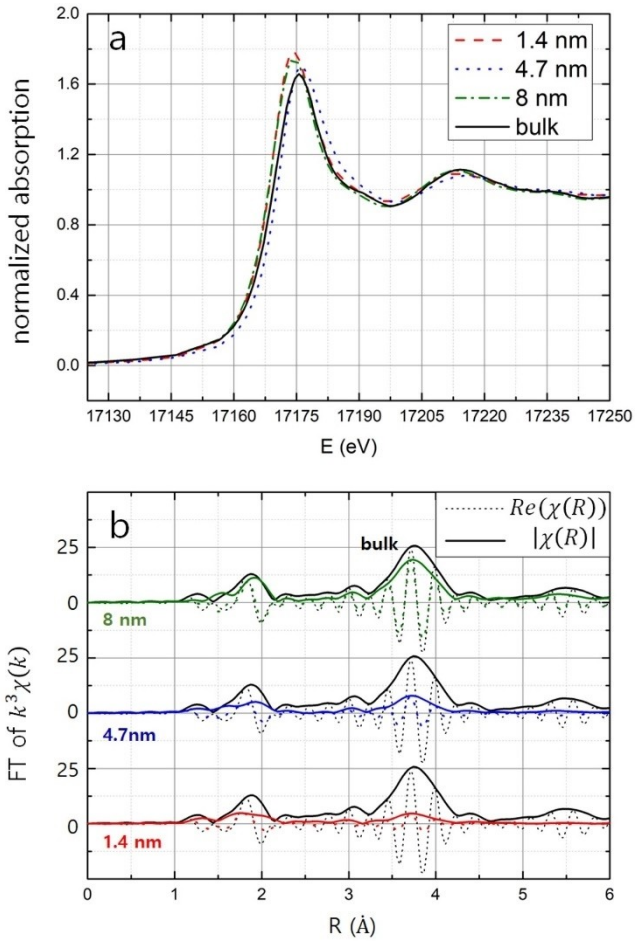

Figure 1. (a) Normalized XANES spectra and (b) the real part (dotted) and magnitude (solid) of the Fourier-transformed XAFS for 1.4 nm (red), 4.7 nm (blue), 8 nm (green) UO_2 NP compared with bulk UO_2 (black).

An appropriate fitting process involving $\chi(k)$ and $\chi(R)$ was implemented using ARTEMIS[26] to extract accurate structural information. The fitting-extracted parameters are shown in Table 1 and Table S2 and fitting models shown in Figure S2. The change in interatomic distances of U–O and U–U was less than 1.2%, which suggests the geometric change in the crystal structure was insignificant. As expected from the termination effect, CN was smaller for smaller particles. The Debye-Waller factor σ^2 of 1.4 and 4.7 nm NPs were significantly larger than that of 8 nm NPs and bulk material.

Extraction of NP static radial disorder from Debye analysis

NP static disorder was extracted from σ^2 (which contains contributions from both thermal and static disorder) by applying a correlated-Debye model[27] to the fit results from the first and second coordination shells (U–O) and (U–U), respectively, as a function of temperature (Table 2, Figures S2 and S4, Table S3). Details of our analysis process are provided in the Supporting Information. The fitting process removes the thermal contribution to disorder so that radial disorder due to inherent differences in structural bond lengths can be observed. With the exception of comparable static disorder values of the first shell for 1.4 and 4.7 nm NPs within error, decreasing trends in the average static disorder of both first shell (U–O) and

Table 1. EXAFS fitting-extracted parameters(50 K). Fitting details and additional parameters can be found in the supporting information.

NP size	Path	CN	R (Å)	σ^2 (Å^2)
1.4 nm	U–O	7.2±0.6	2.341±0.009	0.01±0.01
	U–U	4±1	3.854±0.008	0.004±0.001
4.7 nm	U–O	7.5±0.6	2.340±0.007	0.011±0.002
	U–U	5.3±0.7	3.859±0.004	0.0025±0.0006
8 nm	U–O	8.0±0.5	2.360±0.007	0.004±0.001
	U–U	10±2	3.871±0.003	0.0015±0.0006
Bulk	U–O	8±1	2.341±0.008	0.003±0.001
	U–U	12±2	3.866±0.004	0.0008±0.0004

Table 2. Fitted static disorder and correlated-Debye temperatures.

NP size	Path	σ_{static}^2 (Å^2)	Debye T (K)
1.4 nm	U–O	0.008±0.001	900±200
	U–U	0.0031±0.0007	400±100
4.7 nm	U–O	0.009±0.001	900±200
	U–U	0.0020±0.0004	500±100
8 nm	U–O	0.0031±0.001	1000±400
	U–U	0.0010±0.0003	340±30

Research Article
doi.org/10.1002/ejic.202200417

second shell (U–U) were observed. In all cases, the disorder values extracted are greater than those observed for even combined radial and thermal disorder in bulk. This result suggests that either reduced size or increased surface contributions lead to enhanced structural disorder.

Quantification of surface-terminating species

The termination effect, or reduction in coordination number due to a reduction in coordination at the surface, was employed to quantify the surface terminating species of UO_2 NPs (namely whether the surface is terminated with open U-sites or if oxygen fully shields surface-adjacent uranium). To create an effective model, a few key assumptions were required. First, the NPs were assumed to be ideally spherical. Although in practice NPs are not perfect spheres, TEM images (Figure S1) revealed no substantial anisotropy. Therefore, the NPs can be approximated on average as a sphere. Second, NPs were assumed to be single-faceted, even though the lowest energy structure is often multi-faceted, even for quasi-spherical particles.[28] Still, quasi-spherical NPs are generally dominated by the single, lowest energy facet, making a single-facet assumption generally acceptable.[29] Additionally, a single-facet assumption gives useful insight since a) a consistent trend between NP sizes is observed regardless of the specific surface orientation, and b) because the actual surface will be a combination of multiple facets with different orientations, this extreme single-facet assumption can provide upper- and lower-limit boundaries for expected surface-terminating species distributions. To this end, the three lowest energy surfaces of UO_2, (1 1 1) < (1 1 0) < (1 0 0) were considered.[30] Finally, the UO_2 NP surfaces were assumed to resemble those of bulk UO_2 for the purpose of our calculations, which does not fully account for potential defects. Average structural trends suggest that the overall structure is not greatly different from bulk on average. For instance, the lattice parameter of bulk was used for NPs since the EXAFS results for R are similar within error (Table 1).

A new parameter α was introduced to quantify possible deviation of the NP surface U's CN from the bulk surface U's CN (Figure 2). If the NP surface U has the same coordination environment as bulk surface U, CN_{nano}, the average CN of U atoms in the NP would be: $CN_{nano} = f_1\ CN_{core} + f_2\ CN_{surf}$, where f_1 and f_2 are the relative population of core and surface U atoms, CN_{core} is the CN of the U atoms in bulk core and CN_{surf} is that of the U atoms on a bulk surface. The relative population f_1 and f_2 are determined by dividing the number of core U atoms and surface U atoms with the total number of U atoms in the NP (see supporting information for detailed calculation). CN_{core} is 8 and CN_{surf} for bulk (1 1 1), (1 1 0) and (1 0 0) surfaces are 7, 6 and 8 respectively.[30]

It was hypothesized, however, that CN_{nano} may deviate from $f_1\ CN_{core} + f_2\ CN_{surf}$, due to differences in the coordination environment between the U atoms on NP and bulk surfaces. NP core U atoms were assumed to have the same CN as bulk core U, while the CN of the atoms on NP surface was expected to deviate from that of bulk surface atoms due to curvature and energetic effects which may affect the stoichiometry. A new parameter α quantifies this deviation, so that the CN of the NP surface U is αCN_{surf} rather than CN_{surf}. As a result, the termination effect can be expressed as the following equation (1):

$$CN_{nano} = f_1\ CN_{core} + f_2\ \alpha CN_{surf} \quad (1)$$

Namely, an α value of 1 demonstrates no deviation from expected bulk surface CN whereas a value greater or less than 1 signifies deviation.

The value of α was evaluated for each NP size and for each surface orientation (Figure 2). There was an increase in α in the 4.7 to 8 nm region for all surface orientations (this increase is notably within error). The error of α increased with increasing NP size. Although it isn't possible to differentiate between the potential facets from these results, the results provide the potential range of α for these NPs. Overall, regardless of size or surface facet, the value of α did not deviate substantially from 1, which suggests the structural resemblance of NP surface to bulk surface.

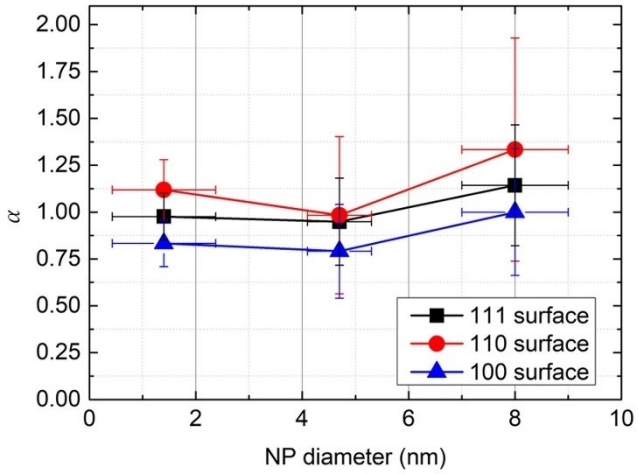

Figure 2. α evaluated for NPs of varying size and surface faceting. α of bulk is always 1 (regardless of surface facet) according to its definition.

Simulating the effects of NP surface layer structure

EXAFS simulations were implemented to account for potential differences in U–O bond length and disorder that might occur in surface layers compared with the NP core, which is expected to more greatly resemble bulk UO_2. The equation used for the first-shell EXAFS simulation of the first shell (which corresponds to the U–O path in this case) is equations 2–3:[15d,19]

$$\chi(k) = \int_{r_{min}}^{r_{max}} \chi(k,r)\rho(r)dr \quad (2)$$

Research Article
doi.org/10.1002/ejic.202200417

$$\text{where } \chi(k,r) = \frac{S_0^2}{kr^2} f(k) e^{-2r/\lambda(k)} \sin[2kr + \delta(k)] \quad (3)$$

The reduction factor S_0^2 is set to 1, and functions for the scattering amplitude $f(k)$, mean free path $\lambda(k)$, and phase $\delta(k)$ were acquired from the FEFF6 calculation of cubic fluorite UO_2. $\rho(r)$ is the distribution of U–O distances, as derived using inputs from the NP structure. In typical EXAFS analysis, as reported above, $\rho(r)$ is defined as a Gaussian. In our simulations below, rather than using a fixed distribution, the distribution varies out from the NP core to its surface.

The NPs were assumed to be spherical, and their structures were defined with two parameters: 1) the distance between U and O atoms $r(\tilde{R})$ and 2) its variance $\sigma^2(\tilde{R})$, where $\tilde{R}$ is the distance from the NP's center to the U atom of interest. These user-defined $r(\tilde{R})$ and $\sigma^2(\tilde{R})$ values were used to acquire $\rho(r)$, assuming the distances from the U atom to the neighboring O atoms follows a Gaussian distribution of mean value $r(\tilde{R})$ and variance $\sigma^2(\tilde{R})$.

In this model, the surface of NPs was assumed to be terminated with the lowest energy, (1 1 1) surface facet. Among various factors that may affect surface structure, we aimed at modeling the surface reconstruction of the UO_2 NP. Surface reconstruction is a thermodynamically driven process, which can exist for systems without significant surface ligand binding interactions,[19,30–31] and is the case for the NP system discussed here. To stabilize the surface energy, the bonds near the UO_2 surface are known to contract, as determined by Rutherford Backscattering Spectroscopy (RBS) and computation.[30,31b, 32] For bulk UO_2, the U–O bond length on the (1 1 1) surface is 2.324 Å, which is smaller than the 2.368 Å of the reported U–O bond length of bulk interior atoms.[30,31b, 32]

The U–O bond length at the NP center was assumed to be the same as the bond length observed in bulk interior atoms (2.368 Å) while that on the NP surface was assumed to be the same as the bond length on a bulk UO_2 (1 1 1) surface. Four scenarios of $r(\tilde{R})$ were considered to describe the U–O bond length distribution in the NPs (Figure 3). This allows for simulation of the degree in which relaxation at the NP surface might affect atoms in near-surface or interior layers. Under the first scenario $r(\tilde{R})$ decreased linearly with increasing $\tilde{R}$. The second scenario followed the 'deep penetration' curve where surface relaxation affected (or penetrated) deeply into the core of the NP so that $r(\tilde{R})$ was smaller than $r(\tilde{R})$ predicted by the linearly decreasing scenario. The third and fourth scenarios followed the 'shallow' and 'very shallow penetration' curves where the surface relaxation only affected the bonds in the first two or one layers near the surface. The shallow and very shallow penetration curves were adjusted to pass through ($\tilde{R}^*$, r^*), where $\tilde{R}^*$ was the distance from the NP's center to the two or one interplanar spacings of U (1 1 1) from the surface and r^* the point which internally divided the uncontracted (unaffected) bond length and fully contracted bond length in the ration 1 : 9 (See supporting information for details).

As for the local disorder, four scenarios of $\sigma^2(\tilde{R})$ have been considered. In all cases, the disorder at the NP center was assumed to be same as the static disorder determined experimentally for bulk UO_2 ($\sigma^2_{bulk} = 0.003 Å^2$) (Figure 4). The first scenario assumed that the disorder of the NP did not change with increasing $\tilde{R}$, with its value fixed at σ^2_{bulk}. Two scenarios assumed higher surface disorder at the NP surface, where $\sigma^2(\tilde{R})$ increased linearly with increasing $\tilde{R}$, the surface disorder being 1.5 σ^2_{bulk} and 3 σ^2_{bulk}. The last scenario assumed that $\sigma^2(\tilde{R})$ decreased linearly with increasing $\tilde{R}$, the surface disorder being 0.5 σ^2_{bulk}.

The U–O distance distribution $\rho(r)$ was determined for each NP based on the structure defined by these scenarios. Figure 5 represents example resulting average $\rho(r)$s simulated for 4.7 nm NPs. It was observed that as the surface relaxation penetrated deeper into the NP, the distributions were shifted

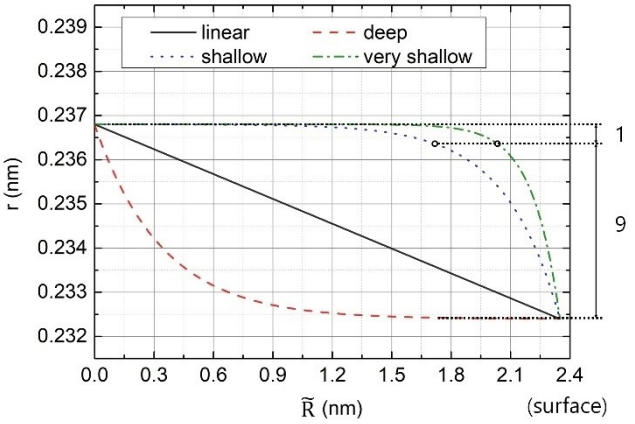

Figure 3. U–O distance vs. radial position used in simulating 4.7 nm NPs from the interior (0) to surface (2.35) nm. Surface relaxation effects are considered which vary in potential penetration into the NP core. The circles mark ($\tilde{R}^*$, r^*) or the intersections between the shallow and very shallow curves with the line that divides the uncontracted bond length and fully contracted bond length in the ratio 1 : 9.

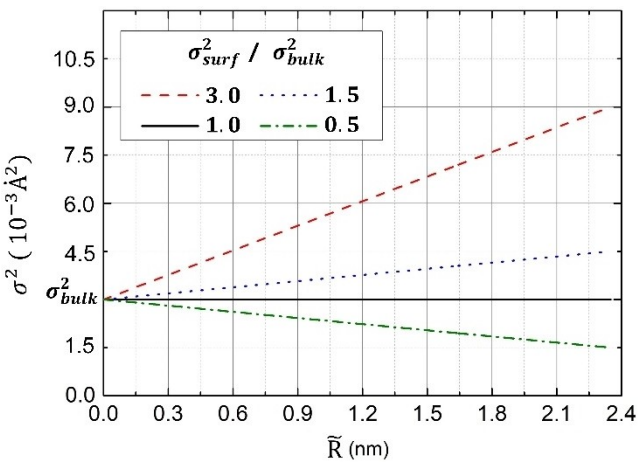

Figure 4. U–O disorder vs. radial position used in simulating 4.7 nm NPs. In all cases, the NP interior disorder was assumed to be the same as that observed in bulk UO_2 (0 nm) and was varied linearly out to the NP surface (2.35 nm).

Research Article
doi.org/10.1002/ejic.202200417

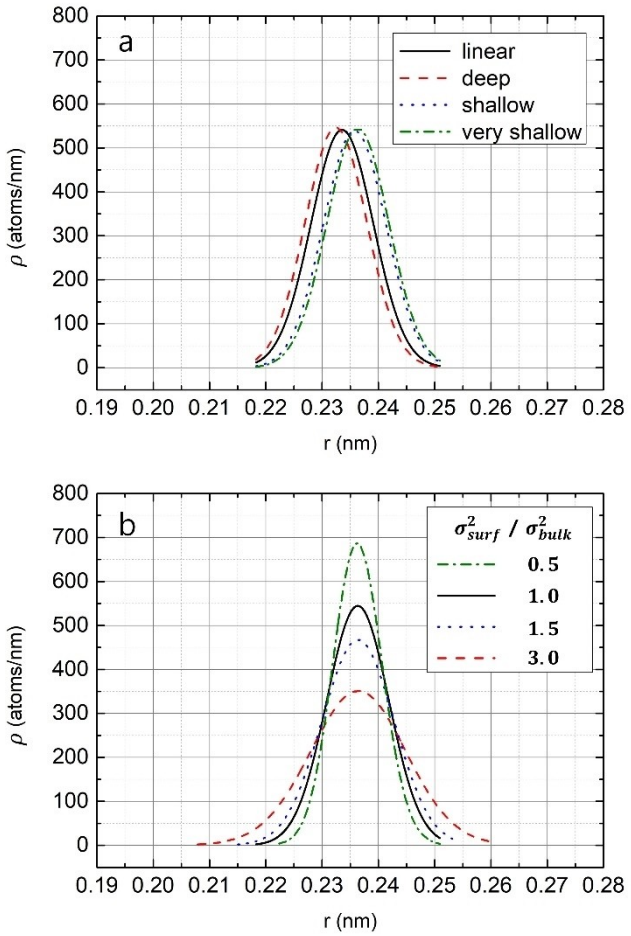

Figure 5. Example U–O radial distributions for 4.7 nm NP of (a) various $r(\tilde{R})$ cases with $\sigma^2_{surf} = \sigma^2_{bulk}$ and (b) various $\sigma^2(\tilde{R})$ cases with $r(\tilde{R})$ following the 'very shallow penetration' curve.

toward shorter *r* (Figure 5a), and as the surface disorder increased, the distributions were broadened (Figure 5b).

EXAFS simulations were generated for all $\rho(r)$ using equations 2–3 and fit with Artemis[26] (see code in supporting information). The *k* range and *r* range used in the simulated EXAFS fitting were the same as the range used to fit the experimentally acquired EXAFS signals. Artemis uses the Gaussian approximation to find the best-fit CN *N*, the average distance *r*, and disorder σ^2 according to the following equation (4):

$$\chi(k) = \frac{NS_0^2}{kr^2} f(k) e^{-2k^2\sigma^2} e^{-2r/\lambda(k)} \sin[2kr + \delta(k)] \quad (4)$$

In the simulated EXAFS fitting, *N* was fixed to the CN values extracted from experimental EXAFS via *ab-initio* modeling. Both experimental and simulated spectra were directly fit with ARTEMIS to determine the average distance *r* and disorder σ^2 for each spectrum. The simulated EXAFS signal of bulk UO_2 was fit in advance to obtain the reduction factor, S_0^2, which gives the correct *N* for the bulk UO_2 structure. S_0^2 was found to be 1.033 and was fixed at this value for the rest of the fits.

The average U–O distance *r*, and disorder σ^2 were found for all generated EXAFS signals (Table S5). Figure 6 illustrates the fitting results of EXAFS signals generated from user-defined simulations for the 4.7 nm NP U–O distance distributions as described above. It was observed that as the surface relaxation penetrated deeper into the NP, *r* for the average U atom was shortened and as the surface disorder increased, σ^2 for the average U atom increased.

Discussion

Oxygen termination of UO_2 NPs@COF-5

By introducing α into the termination effect, the CN of U atoms on the NP surface can be extracted from EXAFS. Notably, in all cases, α does not drastically deviate from 1. This suggests that the surface is indeed terminated by O atoms, which mimics the structure observed in bulk. This result has previously been suggested for AnO_2 NPs with either a lack of or weak-binding surface ligands.[18f,22] The observed result also provides support that the NP surface layers are unlikely to contain super-stoichiometric UO_2. A slight increase in α in the 4.7 to 8 nm region for all surface orientations is observed (is notably within error). If real, the result may suggest that additional terminal oxygen is required for larger NPs, which still exhibit high energy surfaces but may have a reduced concentration of surface defects that could otherwise compensate for energetically unfavorable surface layers. To further consider this trend, additional NP sizes (particularly in the range larger than 5 nm) need to be investigated and compared.

The error of α was significantly large as expected, given the relatively large error bars typically associated with EXAFS-extracted CN. The uncertainty was further amplified when

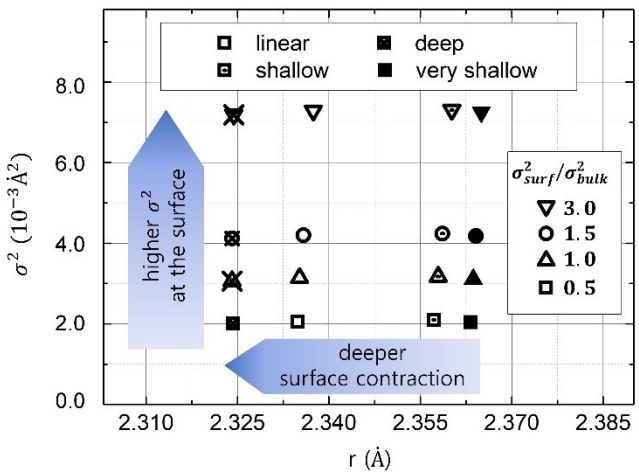

Figure 6. The EXAFS fitting results (U–O average distance and disorder) for the various simulated first nearest-neighbor distributions of 4.7 nm NP. Errors for the fitting results are negligibly small compared to the size of the symbol (supporting information).

Research Article
doi.org/10.1002/ejic.202200417

applying the termination effect. It was observed that the error of α increased with increasing NP size. This was because the relative population of surface U atoms to the total number of U atoms within the NP decreases with increasing NP size. This trend has also been observed in other studies involving termination effect: the amplification of error for larger NPs limits the scope of termination effect-based size determination to very small NPs.[18a–e] Still, despite the degree of error, it is worthwhile to contrast NP and bulk surface terminating species, and this model can be also applied to systems where it may be more ambiguous which species would be energetically expected to terminate NP surface facets.

The origin of disorder within UO_2 NPs@COF-5

Debye analysis shows that the NPs display significant radial disorder compared to bulk UO_2, but the origin of this disorder remains unclear using Debye analysis alone. Results from our user-defined EXAFS simulations provide insight into observed trends. In particular, we aimed to determine whether increased disorder can be attributed solely to relaxation of surface layers or if additional amorphization is observed, and if there is any difference in core vs. surface layers to this end.

Figure 7 plots the simulated EXAFS spectra which yield the closest values of r and σ^2 to the experimental EXAFS (Figure 8). The discrepancies between simulation and experiment may originate from the inaccuracy in $\rho(r)$, which can be attributed to some of the assumptions that were made in this model. First, it may be erroneous to assume that the U–O bond length at a specified point followed the Gaussian distribution of mean value $r(\tilde{R})$ and variance $\sigma^2(\tilde{R})$. The use of this assumption was unavoidable because we wanted to keep the definition of disorder consistent with that of the EXAFS-fitting disorder, as described in equation 4. Furthermore, the discrepancies might have arisen from the imperfectness of the 'scenarios' for $r(\tilde{R})$ and $\sigma^2(\tilde{R})$. Still, for the most part, the model serves its end in predicting the local structure of NP based on the knowledge of bulk UO_2 structure, given the noticeable similarity between the simulation and experimental EXAFS. Also, although higher oxide formation was not confirmed for the system, as it was a large component of a previous study[22] and would be inconsistent with the EXAFS-derived fitting parameters, we cannot rule out the possibility that a small amount of higher oxide below the detection limit may have caused distortion of $\rho(r)$.

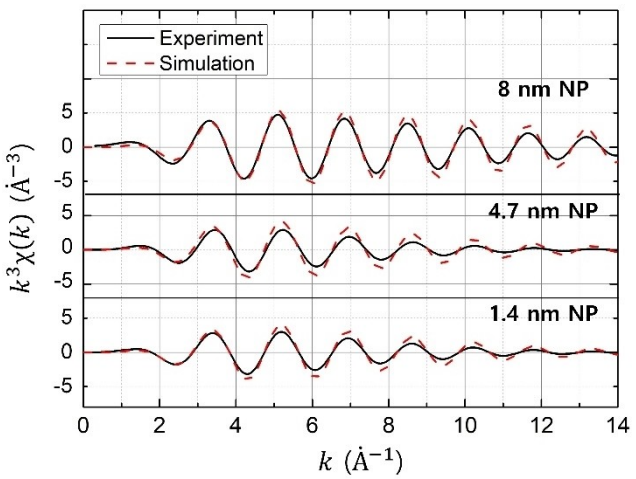

Figure 7. Weighted first shell EXAFS signals acquired by experiments and most representative simulations for 8 nm (top), 4.7 nm (middle), and 1.4 nm (bottom) NPs. The experimental spectra were aligned with adjusted ΔE_0.

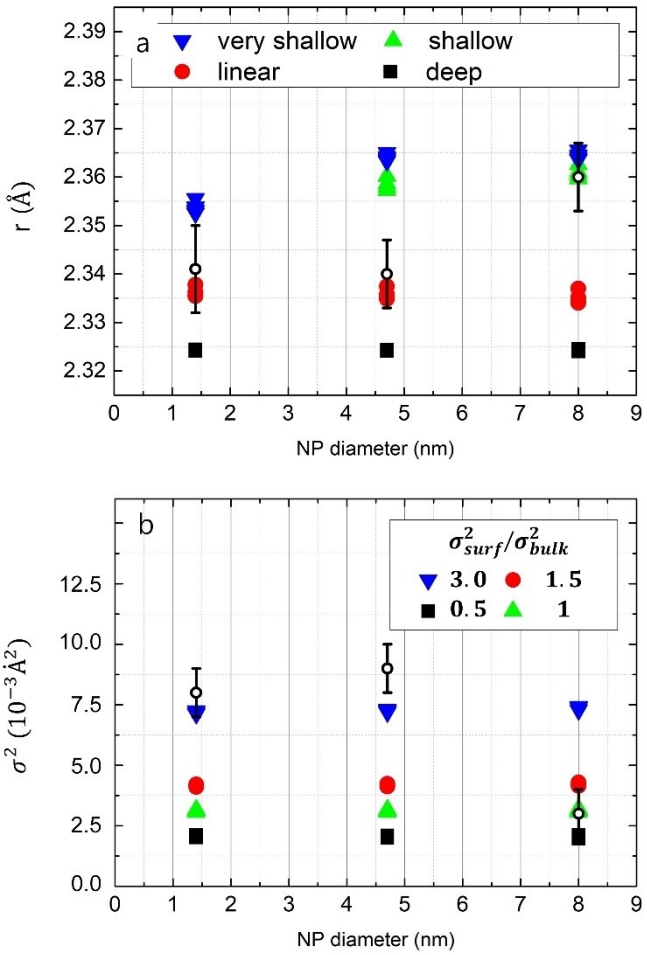

Figure 8. Fitted (a) U–O distance and (b) disorder of simulated EXAFS (solid symbols) and experimentally acquired EXAFS (hollow symbols) for varying NP size. For 1.4 nm NP, the 'linear' scenario and the 'shallow penetration' scenario overlap with the same $r(\tilde{R})$ curve due to the small NP size (Figure S8).

Figure 6 suggests that that the surface disorder contributes significantly less to the fitted value of U–O distance than the degree of surface relaxation penetration into the NP does. As for the disorder, the degree of surface relaxation penetration contributes significantly less to the fitted value of disorder than the surface disorder does. Therefore, the degree of surface relaxation penetration into NPs can be deduced by comparing the fitted U–O distance of simulated and experimentally acquired EXAFS (Figure 8a), while the surface disorder of NPs can be deduced by comparing fitted disorder values (Figure 8b). Because simulations inherently have very small error (as can be

Research Article
doi.org/10.1002/ejic.202200417

confirmed by the negligible error bars of the EXAFS fitting values, refer to the supporting information), the error of U–O distance and surface disorder extracted from the model will directly depend on the error of EXAFS-fitted U–O distance and disorder of UO_2 bulk and NPs from *ab-initio* modeling.

According to the model, Figure 8a suggests that the surface relaxation for the larger, 8 nm NP is mostly limited to the bonds in the first two (shallow penetration) or one (very shallow penetration) U layers. Localization of the relaxation effect on the UO_2 surface was predicted by Tasker's theoretical calculations on bulk UO_2.[31b] For the 1.4 and 4.7 nm NPs, the data suggests that the penetration may propagate further into the NPs (between shallow and linear). The authors are hesitant to place much emphasis on this result considering the fitted value of U–O distance of bulk UO_2 was actually smaller (2.34 Å) than the accepted value of 2.368 Å. Moreover, the insensitivity of surface disorder values to the surface relaxation scenarios, as observed in Figure 6, suggests that the increased static disorder within the UO_2 NPs@COF-5 cannot be explained through surface relaxation effects alone.

As for the surface disorder, Figure 8b suggests that the small (1.4, 4.7 nm) NPs had larger surface disorder than their bulk counterparts ($\sigma^2_{surf} > 3\ \sigma^2_{bulk}$). The surface disorder of 8 nm NP surface was evaluated to be comparable to bulk disorder ($\sigma^2_{surf} \sim \sigma^2_{bulk}$). A discernible decrease of surface disorder was observed with increasing NP size between 4.7 and 8 nm. One possible explanation for this can be attributed to the higher curvature of smaller nanoparticles. Higher curvature adds additional energy to the surface which may enhance amorphization, resulting in higher overall disorder.[33] The slight increase in alpha in this region (Figure 2) may be relevant to this phenomenon. There is a possibility that the additional oxygen attachment on the 8 nm particle lowered the surface energy and hence reduced the amorphization and consequently the surface disorder. Another more plausible source of disorder is the nonstoichiometry of the surface, which leads to a high defect concentration. Previous research in NP amorphization suggest that there is a critical defect density beyond which the amorphous phase starts to form and it decreases with NP size.[34] Thus, the higher degree of disorder for smaller particles can be attributed to the formation of amorphous phase due to lower critical defect density. Regardless of the origin of the much-increased disorder in sub-5 nm vs. 8 nm particles, this suggests that there may be a critical size within this range under which longer-range order effects become favorable and may correlate with observed properties.

This size-dependent surface disorder suggests that it is inherently impossible to decouple the effects of NP size and surface disorder in the size range investigated. Additional data points beyond 8 nm are needed to confirm the surface disorder of the larger NPs are same as that of their bulk counterparts. Also, additional data points between 4.7 and 8 nm can reveal if the marked decrease of UO_2 surface disorder was gradual or abrupt. The surface disorder transition in such a small range can be advantageous in extracting the pure size dependency of NP's physicochemical properties such as magnetic coercivity or superconductivity transition temperature of NPs which are known to occur in the few tens to hundreds of nanometers in length scale.[35] It is therefore surprising to observe such similarity to bulk UO_2 within size regimes smaller than when bulk-like behavior is typically expected to emerge. Moving forward, the ability of this model to quantify the surface disorder will enable a more accurate description of the structural dependent properties of UO_2 NPs which can be correlated with electronic, thermal and magnetic properties of interest to future studies.

Advantages and limitations of the user-defined two-parameter model

It should be noted that isotropic NP system can be modeled using our approach by varying $r(\tilde{R})$ and $\sigma^2(\tilde{R})$. Since introduced by Yevick,[19] EXAFS simulations involving atomistic simulations have been more broadly implemented to determine the structure of various NPs.[20–21] In spite of the high accuracy and precision of those models, the rigorous computation of the interactions between the atoms may not always be necessary if the objective is simply to obtain a more thorough understanding of radially-dependent NP structure. Additionally, actinide-based systems in particular benefit from a model that does not rely on atomistic simulations, due to the difficulty in computational prediction of NP structure based on additional complications from spin-orbit coupling and relativistic effects.

The two-parameter model successfully combines with EXAFS and serves its end in predicting the radially-dependent structural attributes of UO_2 NPs. The simplicity of this model allows the modeling of a variety of structures with multiple elements, which adds significant complexity to the computation. The model can additionally be applied to metal oxide systems, semiconductors, and An carbide and nitride systems. However, the application of this method to anisotropic systems such as multifaced or heterogeneously doped NPs will not be trivial because the local disorder cannot be expressed with uniformly representative $r(\tilde{R})$ and $\sigma^2(\tilde{R})$. Another limitation is that there can be multiple $\rho(r)$ that can give the same EXAFS fitting results. Therefore, the ambiguity has to be lifted with scientific intuition.

Conclusion

This study reports the extraction of EXAFS results from UO_2 NPs to obtain surface vs. bulk structural characteristics by modeling which incorporates NP heterogeneity. This enabled us to determine the surface terminating species, U–O bond length and disorder specific to NP surface layers.

The key findings of the study are as follows:

- The CN of U atoms on the NP surface was determined using the termination effect. Overall, the NP surfaces are oxygen-terminated and resemble bulk UO_2 surface compositions. Our presented method to determine deviations in NP vs. bulk

surface termination proves more accurate for ultra-small NP sizes.

- A two-parameter model was developed to simulate radial dependence from the NP core to surface on U–O bond length and radial disorder. Results from user-defined simulation were compared with experimental EXAFS to decouple surface vs. bulk contributions to the overall EXAFS signal.
- The surface disorder of small (1.4, 4.7 nm) NPs were noticeably larger than that of their bulk counterpart, which markedly decreases to the bulk level for 8 nm NPs. This suggests that there may be a critical NP size at which ordering at the surface occurs. Investigation of NPs at additional sizes will assist in confirming this trend. The universality of size-dependent surface ordering can be explored through extending our investigation to other inorganic NP systems.
- Results from this work suggest that increased static disorder in UO_2 NPs@COF-5 cannot be attributed to surface relaxation effects alone. Rather, substantial radial disorder at the surface is observed compared to what would be expected in bulk.
- Overall, we have developed a primitive model to account for heterogeneity to extract surface-dependent information from bulk EXAFS signals. With the ease of considering user-defined trends, this work presents an opportunity to further decouple NP surface structure from bulk. The model can serve as a good first step to structurally characterize inorganic NPs beyond the case of UO_2 with the application of system-appropriate assumptions.

Experimental Section

Sample preparation

The UO_2 NPs@COF-5 were synthesized via thermal decomposition of a molecular precursor embedded in a COF-5 template, as described previously.[22] Decomposition temperatures of 200 °C, 250 °C, and 300 °C were used, providing particle sizes of 1.4 nm, 4.7 nm and 8 nm, respectively, as determined by TEM (Figure S1). The smaller 1.4 nm UO_2 NPs remained confined the COF-5 template, while the larger 4.7 and 8.0 nm NPs showed a tendency for segregation to the surface. Nanoparticle samples were mixed with dry boron nitride in an argon-filled glovebox to ensure a uniform sample of ideal concentration. The diluted samples were then packed into indium-sealed aluminum holders. Due to air and water sensitivity, samples were stored under argon until measurement and sealed holders were exposed to air for less than one minute while being transferred to vacuum with a He backfill. Samples were measured at multiple temperatures (50 K, 100 K, 200 K and 300 K) using a liquid He-cooled cryostat in order to conduct Debye analysis for extraction of radial disorder from thermal contributions.

X-ray absorption fine structure spectroscopy

XAFS data at the U L_3 absorption edge (17.166 keV) were collected at Beamline 11–2 at the Stanford Synchrotron Radiation Lightsource using a Si 220 ($\phi = 0$) monochromator detuned to 50%. Data were collected in fluorescence mode, using a 100 Element Canberra Ge fluorescence detector (sample at 45° from the incident beam and fluorescence detector) and corrected for dead time. Transmission-mode data were collected simultaneously to monitor any potential self-absorption effects. Multiple scans were collected for each sample and compared to confirm that no photoreduction or sample damage was observed over time in the high energy X-ray beam. Edge energies were calibrated by comparing to Zr foil (17.998 keV) and UO_2 (17.170 keV) standards. To ensure that the data resolution was core-hole lifetime limited, a slit height less than 0.7 mm was used. Data were reduced and analyzed using the IFEFFIT software package.[26] The background was removed using the AUTOBK algorithm[36] and data fit in R-space to multiple *k*-weights using theoretical pathways generated by FEFF6. The number of variables varied in the fit were limited to be less than two thirds the number of independent points. Experimental data in k-space are available in Figure S2a.

Acknowledgements

XAFS measurements were collected at the Stanford Synchrotron Radiation Lightsource, which is supported by the U.S. Department of Energy, Office of Science, Office of Basic Energy Sciences under contract no. DE-AC02-76SF00515. TEM images collected at the Molecular Foundry were supported by the Office of Science, Office of Basic Energy Sciences, of the U.S. Department of Energy under Contract No. DE-AC02-05CH11231. A. Knapp was supported by Washington State University through a seed grant from the WSU Office of Research and the Graduate School. This work was supported in part by the Director, Office of Science, Office of Basic Energy Sciences, Division of Chemical Sciences, Geosciences, and Biosciences Heavy Element Chemistry Program of the U.S. Department of Energy (DOE) at LBNL under Contract No. DE-AC02-05CH11231. We would like to thank Ryan Davis for his assistance with XAFS measurements. We also thank Prof. Anatoly Frenkel for helpful discussion.

Conflict of Interest

The authors declare no conflict of interest.

Data Availability Statement

The data that support the findings of this study are available in the supplementary material of this article.

Keywords: Actinide oxides · Heterogeneity · Nanotechnology · Surface analysis · X-ray absorption spectroscopy

[1] C. Walther, M. A. Denecke, *Chem. Rev.* **2013**, *113*, 995–1015.
[2] a) S. N. Kalmykov, M. A. Denecke, *Actinide Nanoparticle Research*, Springer, New York, **2011**; b) P. Liu, X. Luo, M. Wen, J. Zhang, C. Zheng, W. Gao, F. Ouyang, *Appl. Geochem.* **2018**, *97*, 226–237; c) *Radioactive Particles in the Environment: Sources, Particle Characterization and Analytical Techniques*, INTERNATIONAL ATOMIC ENERGY AGENCY, Vienna, **2011**.
[3] J. Spino, H. Santa Cruz, R. Jovani-Abril, R. Birtcher, C. Ferrero, *J. Nucl. Mater.* **2012**, *422*, 27–44.
[4] T. M. Nenoff, B. W. Jacobs, D. B. Robinson, P. P. Provencio, J. Huang, S. Ferreira, D. J. Hanson, *Chem. Mater.* **2011**, *23*, 5185–5190.

[5] a) G. Song, L. Cheng, Y. Chao, K. Yang, Z. Liu, *Adv. Mater.* **2017**, *29*, 1700996; b) M. Toro Gonzalez, A. Dame, S. Mirzadeh, J. Rojas, *J. Appl. Phys.* **2019**, *125*.
[6] a) M. D. Straub, J. Leduc, M. Frank, A. Raauf, T. D. Lohrey, S. G. Minasian, S. Mathur, J. Arnold, *Angew. Chem. Int. Ed.* **2019**, *58*, 5749–5753; *Angew. Chem.* **2019**, *131*, 5805–5809; b) J. Leduc, M. Frank, L. Jürgensen, D. Graf, A. Raauf, S. Mathur, *ACS Catal.* **2019**, *9*, 4719–4741.
[7] a) Q. Yan, Y. Mao, X. Zhou, J. Liang, M. Ye, S. Peng, *J. Nucl. Mater.* **2018**, *512*, 417–422; b) J. Yan, B. K. Teo, N. Zheng, *Acc. Chem. Res.* **2018**, *51*, 3084–3093; c) T. Echigo, D. M. Aruguete, M. Murayama, M. F. Hochella, *Geochim. Cosmochim. Acta* **2012**, *90*, 149–162.
[8] a) M. Salmeron, R. Schlögl, *Surf. Sci. Rep.* **2008**, *63*, 169–199; b) M. Salmeron, *Top. Catal.* **2018**, *61*, 2044–2051.
[9] M. Azubel, J. Koivisto, S. Malola, D. Bushnell, G. L. Hura, A. L. Koh, H. Tsunoyama, T. Tsukuda, M. Pettersson, H. Häkkinen, R. D. Kornberg, *Science* **2014**, *345*, 909–912.
[10] a) M. Baron, O. Bondarchuk, D. Stacchiola, S. Shaikhutdinov, H. J. Freund, *J. Phys. Chem. C* **2009**, *113*, 6042–6049; b) T. Reetz Manfred, W. Helbig, A. Quaiser Stefan, U. Stimming, N. Breuer, R. Vogel, *Science* **1995**, *267*, 367–369.
[11] a) Z. Peng, F. Somodi, S. Helveg, C. Kisielowski, P. Specht, A. T. Bell, *J. Catal.* **2012**, *286*, 22–29; b) H. L. Xin, K. Niu, D. H. Alsem, H. Zheng, *Microsc. Microanal.* **2013**, *19*, 1558–1568.
[12] W. D. Pyrz, D. J. Buttrey, *Langmuir* **2008**, *24*, 11350–11360.
[13] C. F. Holder, R. E. Schaak, *ACS Nano* **2019**, *13*, 7359–7365.
[14] a) L. Amidani, G. B. M. Vaughan, T. V. Plakhova, A. Y. Romanchuk, E. Gerber, R. Svetogorov, S. Weiss, Y. Joly, S. N. Kalmykov, K. O. Kvashnina, *Chem. Eur. J.* **2021**, *27*, 5–5; b) B. Gilbert, F. Huang, H. Zhang, G. A. Waychunas, J. F. Banfield, *Science* **2004**, *305*, 651–654; c) K. Jensen, A. Blichfeld, S. Bauers, S. Wood, E. Dooryhée, D. Johnson, B. Iversen, S. Billinge, *IUCrJ* **2015**, *2*.
[15] a) S. Kobayashi, I. R. M. Kottegoda, Y. Uchimoto, M. Wakihara, *J. Mater. Chem.* **2004**, *14*, 1843–1848; b) J. Rockenberger, L. Tröger, A. Kornowski, T. Vossmeyer, A. Eychmüller, J. Feldhaus, H. Weller, *J. Phys. Chem. B* **1997**, *101*, 2691–2701; c) B. D. Begg, N. J. Hess, W. J. Weber, S. D. Conradson, M. J. Schweiger, R. C. Ewing, *J. Nucl. Mater.* **2000**, *278*, 212–224; d) G. Bunker, *Introduction to XAFS: A Practical Guide to X-ray Absorption Fine Structure Spectroscopy*, Cambridge University Press, Cambridge, **2010**.
[16] a) G. A. Waychunas, *Rev. Mineral. Geochem.* **2002**, *49*, 267–315; b) M. A. Denecke, J. Rothe, K. Dardenne, P. Lindqvist-Reis, *Phys. Chem. Chem. Phys.* **2003**, *5*, 939–946; c) T. P. Trainor, J. P. Fitts, A. S. Templeton, D. Grolimund, G. E. Brown, *J. Colloid Interface Sci.* **2001**, *244*, 239–244.
[17] W. Vogel, L. Timperman, N. Alonso-Vante, *Appl. Catal. A* **2010**, *377*, 167–173.
[18] a) R. B. Greegor, F. W. Lytle, *J. Catal.* **1980**, *63*, 476–486; b) A. I. Frenkel, C. W. Hills, R. G. Nuzzo, *J. Phys. Chem. B* **2001**, *105*, 12689–12703; c) S. Calvin, M. M. Miller, R. Goswami, S. F. Cheng, S. P. Mulvaney, L. J. Whitman, V. G. Harris, *J. Appl. Phys.* **2003**, *94*, 778–783; d) G. Agostini, A. Piovano, L. Bertinetti, R. Pellegrini, G. Leofanti, E. Groppo, C. Lamberti, *J. Phys. Chem. C* **2014**, *118*, 4085–4094; e) N. S. Marinkovic, K. Sasaki, R. R. Adzic, *J. Electrochem. Soc.* **2018**, *165*, J3222-J3230; f) A. Romanchuk, A. Trigub, T. Plakhova, A. Kuzenkova, R. Svetogorov, K. Kvashnina, S. Kalmykov, *J. Synchrotron Radiat.* **2022**, *29*, 288–294.
[19] A. Yevick, A. I. Frenkel, *Phys. Rev. B* **2010**, *81*, 115451.
[20] a) S. W. T. Price, N. Zonias, C.-K. Skylaris, T. I. Hyde, B. Ravel, A. E. Russell, *Phys. Rev. B* **2012**, *85*, 075439; b) Z. Duan, Y. Li, J. Timoshenko, S. T. Chill, R. M. Anderson, D. F. Yancey, A. I. Frenkel, R. M. Crooks, G. Henkelman, *Catal. Sci. Technol.* **2016**, *6*, 6879–6885.
[21] O. M. Roscioni, N. Zonias, S. W. T. Price, A. E. Russell, T. Comaschi, C.-K. Skylaris, *Phys. Rev. B* **2011**, *83*, 115409.
[22] L. M. Moreau, A. Herve, M. D. Straub, D. R. Russo, R. J. Abergel, S. Alayoglu, J. Arnold, A. Braun, G. J. P. Deblonde, Y. Liu, T. D. Lohrey, D. T. Olive, Y. Qiao, J. A. Rees, D. K. Shuh, S. J. Teat, C. H. Booth, S. G. Minasian, *Chem. Sci.* **2020**, *11*, 4648–4668.
[23] B. Kosog, H. S. La Pierre, M. A. Denecke, F. W. Heinemann, K. Meyer, *Inorg. Chem.* **2012**, *51*, 7940–7944.
[24] J. Rothe, C. Walther, M. A. Denecke, T. Fanghänel, *Inorg. Chem.* **2004**, *43*, 4708–4718.
[25] D. D. Koningsberger, R. Prins, *Chemia Analityczna* **1988**, *92*.
[26] B. Ravel, M. Newville, *J. Synchrotron Radiat.* **2005**, *12*, 537–541.
[27] E. Sevillano, H. Meuth, J. J. Rehr, *Phys. Rev. B* **1979**, *20*, 4908–4911.
[28] a) Z. R. Dai, S. Sun, Z. L. Wang, *Surf. Sci.* **2002**, *505*, 325–335; b) L. D. Marks, *Rep. Prog. Phys.* **1994**, *57*, 603–649.
[29] a) C. Jeyabharathi, M. Zander, F. Scholz, *J. Electroanal. Chem.* **2018**, *819*, 159–162; b) M. L. Personick, M. R. Langille, J. Zhang, C. A. Mirkin, *Nano Lett.* **2011**, *11*, 3394–3398; c) N. V. Suramwar, S. R. Thakare, N. N. Karade, N. T. Khaty, *J. Mol. Catal. A* **2012**, *359*, 28–34.
[30] H. Idriss, *Surf. Sci. Rep.* **2010**, *65*, 67–109.
[31] a) R. J. Needs, M. Mansfield, *J. Phys. Condens. Matter* **1989**, *1*, 7555–7563; b) P. W. Tasker, *Surf. Sci.* **1979**, *87*, 315–324.
[32] K. A. Thompson, W. P. Ellis, T. N. Taylor, S. M. Valone, C. J. Maggiore, *Nucl. Instrum. Meth. Phys. Res.* **1983**, *218*, 475–479.
[33] D. C. Sayle, J. A. Doig, S. A. Maicaneanu, G. W. Watson, *Phys. Rev. B* **2002**, *65*, 245414.
[34] a) L. Piot, S. L. Floch, T. Cornier, S. Daniele, D. Machon, *J. Phys. Chem. C* **2013**, *117*, 11133–11140; b) D. Machon, P. Mélinon, *Phys. Chem. Chem. Phys.* **2015**, *17*, 903–910.
[35] a) M. Rajendran, R. C. Pullar, A. K. Bhattacharya, D. Das, S. N. Chintalapudi, C. K. Majumdar, *J. Magn. Magn. Mater.* **2001**, *232*, 71–83; b) M. S. Multani, P. Guptasarma, V. R. Palkar, P. Ayyub, A. V. Gurjar, *Phys. Lett. A* **1989**, *142*, 293–299.
[36] M. Newville, P. Līviņš, Y. Yacoby, J. J. Rehr, E. A. Stern, *Phys. Rev. B* **1993**, *47*, 14126–14131.

Manuscript received: June 29, 2022
Revised manuscript received: October 25, 2022
Accepted manuscript online: October 26, 2022